Lorentz microscopy of vortex lattices (flux lines) in niobium

J. E. Bonevich, K. Harada, H. Kasai, T. Matsuda, and T. Yoshida
Advanced Research Laboratory, Hitachi, Ltd., Hatoyama, Saitama 350-03, Japan

G. Pozzi
Advanced Research Laboratory, Hitachi, Ltd., Hatoyama, Saitama 350-03, Japan
and Department of Physics, University of Bologna, via Irnerio 46, 40126 Bologna, Italy

A. Tonomura
Advanced Research Laboratory, Hitachi, Ltd., Hatoyama, Saitama 350-03, Japan
(Received 12 November 1993)

Observations of the flux-line lattice in tilted superconducting specimens by standard methods of Lorentz microscopy can be understood in terms of a simple model which (i) first approximates the individual vortex line by a flux tube of negligible radius, thereby obtaining an analytical expression for the two-dimensional phase shift, and then (ii) takes into account the finite flux core structure by convoluting the former expression with the assumed model for the core. By taking the London model for the magnetic-field distribution of the core, thus having the vortex described by a single parameter, i.e., the London penetration depth, the most relevant contrast features observed in the experimental out-of-focus images of a Nb superconductor are interpreted.

I. INTRODUCTION

Recently, observations of quantized flux lines in thin superconducting specimens have been successfully carried out in transmission electron microscopy by means of standard Lorentz microscopy methods for both conventional[1] and high-T_c materials[2] and by electron holography.[3] Although a previous theoretical analysis (reviewing also the work done until 1972) considering the case of fluxons in a thin specimen lying perpendicular to the electron beam predicted the feasibility of such experiments,[4] no successful attempts have been reported until now.

In the meantime, many methods have been used to detect the presence of quantized magnetic-flux lines (henceforth called fluxons or vortices) in superconducting specimens. Static images of the vortices are provided by the Bitter magnetic decoration,[5,6] scanning tunneling,[7] and scanning electron[8] microscopies. Electron holography[9] has been used previously to study the dynamic behavior of magnetic fields near the surfaces of superconductors,[10–12] but the two-dimensional (2D) vortex lattice could not be observed. A magneto-optical technique has been developed that time resolves the flux distribution, although individual vortices were not observed.[13] And Scanning Hall probes have been used to resolve individual vortices,[14] where the surface field perturbation is related to the flux distribution.

In spite of these advances, the possibility of using transmission electron microscopy still opens exciting perspectives both for the direct and dynamical observation of the flux lines and their correlation with structural defects present in the thin foils. Furthermore, the quantitative evaluation of the results obtained by advanced holographic techniques may provide an answer to more fundamental questions such as the degree of flux quantization.

It should be remarked that the recent breakthrough in observing fluxons has been possible due to the introduction of a new geometry, different from those analyzed previously;[4,15] namely, the specimen is observed tilted with respect to both the vertically incident electron beam and the horizontal ancillary magnetic field used to introduce and stabilize the fluxons.[16]

From the wave-optical point of view, this case is complicated with respect to the former ones because the electrons experience both the internal and external field and the resulting phase shift is two dimensional. Nonetheless, it has been shown that when the fluxon is modeled by a flux tube of negligible radius, a simple analytical solution exists for the field and for the phase shift suffered by the electron beam.[16] This elementary solution has then been used as a building block to investigate more realistic models taking into account the fluxon core structure, such as that proposed by London, by approximating it with a suitable arrangement of flux tubes.

Therefore the aim of this paper is to show that this model can be used to account for the most relevant features of the experimental results obtained by the out-of-focus method (Lorentz microscopy). In the following sections, first the experimental methods and results are reviewed; then, the proposed model is briefly recalled and applied to the interpretation of the out-of-focus patterns.

II. EXPERIMENTAL METHODS AND RESULTS

The experiments were conducted in a 300-kV holography electron microscope developed to provide a highly coherent and bright source of electrons.[17] The microscope is equipped with a specially constructed cold stage to allow magnetic fields to be applied while the specimen,

tilted at an angle $\alpha=45°$ with respect to the beam and the magnetic field, is maintained at 4.5 K (see Fig. 1). Three coils are used to apply the magnetic field: The uppermost coil applies the desired field to the specimen (150 G maximum), and the two subsequent coils are used to compensate the deflection of the incident electrons and bring them back to the microscope optic axis. This cold stage enables the user to observe superconductors under both equilibrium and dynamic conditions.

The thin-foil (70±20 nm) specimens used for transmission observation were prepared by chemically polishing 2×2-mm^2-wide by 7-μm-thick Nb [$T_c=9.2$ K, resistance ratio $R(300\text{ K})/R(10\text{ K})\approx20$] sections that had been annealed to ~2000 °C in a vacuum of 10^{-6} Pa. The annealing resulted in a grain size of 200–300 μm with a [110] texture.

The specimen was cooled to 4.5 K in a field of 10 G in order to have a large enough vortex separation (lattice spacing ~1.5 μm), to consider them as isolated. The observations were carried out with the objective lens switched off and the first intermediate lens acting as the imaging lens. Under these conditions an electron optical magnification of $\sim2000\times$ is obtained, allowing very large areas of the specimen to be observed, typically 50 μm in diameter.

Figure 2 reports a through-focus series from a rather thick region of the specimen. Bend contours are present as a result of the slight deformation of the self-supporting thin foil. It can be seen that each vortex is imaged as a tiny globule, one side bright and the other side dark, whose dimensions and contrast increase with increasing defocus distance. The dividing lines of different vortices are nearly parallel, as the vortices have arranged themselves along the direction of the applied magnetic field. The micrograph at the lowest defocus, where vortices are hardly detectable, shows another interesting feature, namely, an elongation of the vortices along a direction slightly different from that of the applied field. Possible reasons for this effect are the presence of distortions due to inhomogenities in the magnetic field of the cold stage and astigmatism of the intermediate lens; however, the theoretical analysis of the following sections suggests another interpretation based on the finite thickness of the specimen.

III. THEORETICAL MODEL

In the standard high-energy or phase-object approximation, only the phase distribution of the incoming electron wave function is modified when electrons pass through a magnetic specimen.[18] That is, a fluxon is a perfect phase object and the magnetic phase shift is given by

$$\varphi=(-2\pi e/h)\int_L \mathbf{A}\,ds\ , \tag{1}$$

where the integral is taken along a straight line L corresponding to the classical electron trajectory, $\mathbf{A}$ is the magnetic vector potential, and e and h the absolute value of the electron charge and Planck constant, respectively.

It is worthwhile to point out that this two-dimensional phase distribution, completely describing the interaction between the fluxon and electron beam, is defined on a plane, the observation plane, perpendicular to the elec-

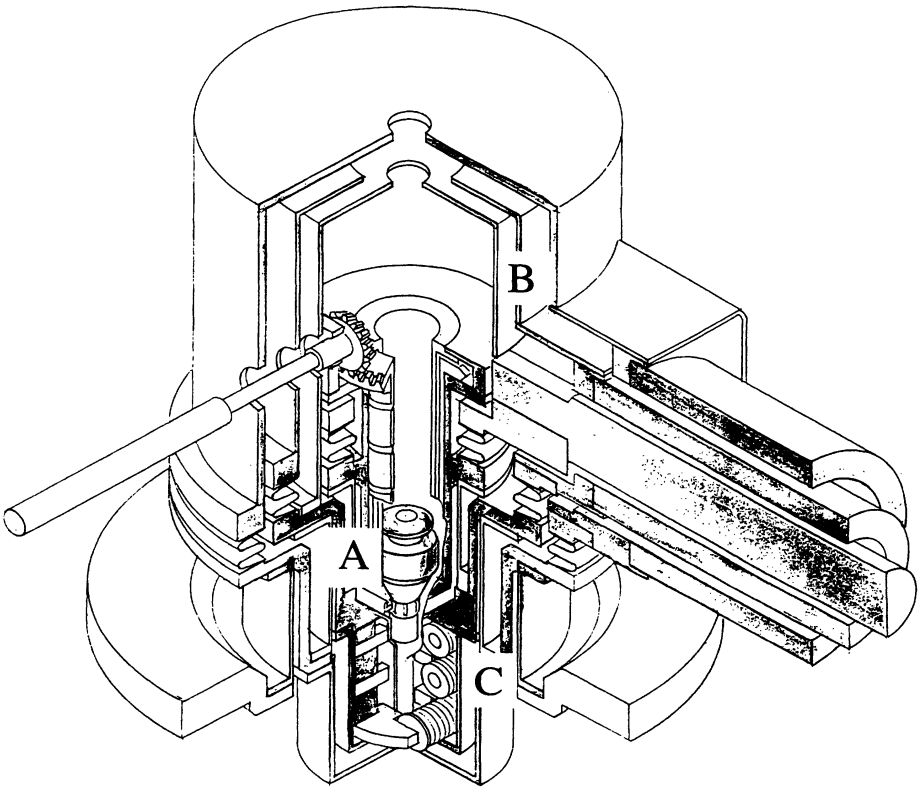

FIG. 1. Diagram of the cold stage. A tilted superconductor is inserted in the specimen holder (A). Cooling shields (B) maintain the specimen down to 4.5 K while magnetic fields (C) may be applied. Stage heaters vary T up to 26 K.

tron beam and whose position along the z axis is not rigorously determined, but is taken coincident with the specimen plane.

The difference of the phase shift between two classical trajectories L_1 and L_2, passing through points 1 and 2 in the object plane, can be expressed by Stoke's theorem as

$$\Delta\varphi=(-2\pi e/h)\int_{S_{12}} B_n dS \ . \tag{2}$$

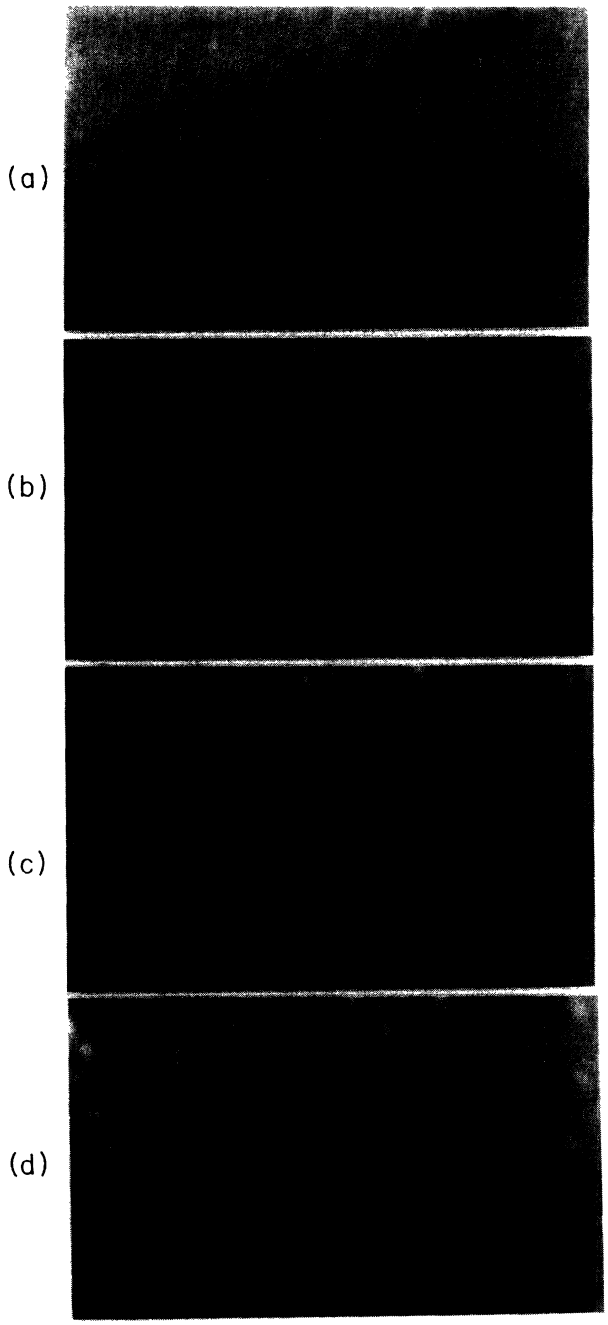

FIG. 2. Vortices in Nb at 4.5 K and 10 G. Through focus series (a)–(d) of 8, 15, 21, and 35 mm defocus. Individual vortices manifest themselves as globules of bright and dark contrast. Note that vortices in (a) appears slightly elongated as a result of the thickness of the specimen. Dark lines are bend contours in the thin foil. The scale bars indicate 0.5 μm.

Since B_n is the component of the magnetic-flux density normal to the surface S_{12} enclosed by L_1 and L_2, the integral stands for the magnetic flux passing through S_{12}.

This second form of the phase shift has been used in Ref. 16 to calculate analytically the phase shift for a flux tube of negligible radius carrying the quantum flux $\Phi=h/2e$ lying perpendicular to the two surfaces of an ideal superconducting specimen of thickness t, inclined at an angle α with respect to the optic axis z (Fig. 3).

In this case the magnetic field in the upper and lower half-spaces is equivalent to that produced by two magnetic poles of strength $\pm\Phi$, respectively, whereas in the perfectly diamagnetic specimen the field is everywhere zero except in the flux tube core.

By considering that the upper and lower poles (i.e., the exit and entry points of the flux tube) have projected coordinates $(a,0)$ and $(-a,0)$ on the object plane [where $a=t\sin(\alpha)/2$; see also the lower part of Fig. 3], the expression for the phase shift is given by

$$\begin{aligned}\varphi(x,y,a,\alpha)=&\frac{1}{2}\arctan\left[\frac{y}{x+a}\right]-\frac{1}{2}\arctan\left[\frac{y}{x-a}\right]\\&+\frac{\pi}{4}\operatorname{sgn}\left[\frac{y}{x-a}\right]-\frac{\pi}{4}\operatorname{sgn}\left[\frac{y}{x+a}\right]\\&-\frac{1}{2}\arcsin[y\sin\alpha/\sqrt{y^2+(x+a)^2}]\\&-\frac{1}{2}\arcsin[y\sin\alpha/\sqrt{y^2+(x-a)^2}].\end{aligned} \tag{3}$$

A contour-line map of the phase shift of the flux tube is sketched on the object plane in the lower part of Fig. 3.

By overlapping a suitable distribution of flux tubes, we

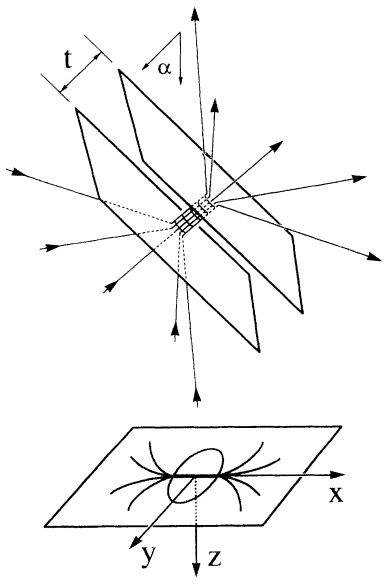

FIG. 3. Coordinate system used to calculate the phase shift due to the flux tube. A specimen of thickness t containing a single flux quantum is inclined by an angle α to the optic axis (upper part); the corresponding phase shift in the object plane is depicted by a contour line map in the lower part.

can approximately model any flux core structure, in the same spirit as in electrostatics where a given field can be approximated by a suitable arrangement of point charges.

In this work we assume that the model describing the fluxon magnetic core within the specimen is given by the London equation

$$B=\frac{\Phi}{2\pi\lambda_L^2}K_0(r/\lambda_L)\ , \tag{4}$$

where K_0 is the zero-order Bessel function, r the radial distance from the fluxon axis, and λ_L the London penetration depth. Therefore the previous expression for the phase shift due to the flux tube is convoluted with the two-dimensional projection in the object plane of the London model, in order to find the corresponding phase shift $\varphi_L(x,y,\alpha,t,\lambda_L)$.

The results are shown in Fig. 4, whose upper part reports the phase shift φ [Eq. (3)] for a flux tube in a specimen of thickness 60 nm, tilted at 45° with respect to the beam and to the ancillary magnetic field, whereas the lower one reports the corresponding phase shift φ_L for a London fluxon with $\lambda_L=30$ nm, i.e., $\lambda_L=t/2$.

It should be noted that whereas in the first case the maximum phase difference across the fluxon core is π, corresponding to the Aharonov-Bohm effect due to the flux tube core, for the specimen of finite thickness the phase is broadened and no longer reaches the value of π corresponding to the flux quantization.

This unexpected effect is displayed more clearly in Fig. 5, where the phase shift across the fluxon at its center is displayed for increasing values of the London length, ranging from zero (flux tube case) to 30 nm. From this figure it can be ascertained that the broadening due to the finite core effects severely dampens the maximum phase difference and smoothes the slope at the core. It should also be noted that at large distances from the core, the phase difference becomes $\pi/2$ irrespective of the London wavelength.

Geometrical reasoning[3] as well as the analysis of the London phase shift[16] show that this phase difference (which in the more general case of tilt by an angle α is given by α itself) is still present even if the distance between the two poles vanishes, which corresponds to a specimen whose thickness is much lower than λ_L: This is another unexpected effect due to this unusual geometry, confirming that the main contribution to the phase shift is due to the external fringing field extending in the two half-spaces above and below the perfectly diamagnetic superconducting film.

IV. CALCULATION OF THE OUT-OF-FOCUS IMAGES

The solution of the Schrödinger equation in the space below the specimen may be given in the paraxial approximation in the form of a Kirchhoff-Fresnel integral[19]

$$\psi(X,Y,Z_0)=\frac{\exp(i\beta)}{(\lambda Z_0)}\int\int \exp i\left[\frac{\pi}{\lambda Z_0}[(x-X)^2+(y-Y)^2]+\varphi_L(x,y,\alpha,t,\lambda_L)\right]dx\,dy\ , \tag{5}$$

where x and y are the coordinates in the object plane, X and Y the coordinates in the out-of-focus plane at a defocus distance Z_0 from the object plane, λ the de Broglie wavelength of the incident electrons, and β a phase factor of no value in the present case as here only the intensity in the image plane is relevant, which is proportional to $|\psi|^2$.

Taking λ_L as the scale length and noting that the London phase shift is a function of x/λ_L, y/λ_L, t/λ_L, and α, it turns out that the intensity in the image acquires the functional form

$$I=I(X/\lambda_L,Y/\lambda_L,\lambda Z_0/\lambda_L^2,t/\lambda_L)\ . \tag{6}$$

Although calculations are carried out for realistic values of the various parameters, the adoption of these dimensionless parameters is convenient because the results obtained are of general applicability, independent of the material, whose superconducting properties are given, in the approximations used, by the single parameter λ_L.

Figure 6 shows a focus series calculated for the case of a specimen having London length 30 nm (of the same order as that of Nb), thickness 60 nm, i.e., $2\lambda_L$, at the following values of the defocus: (a) 1 mm, (b) 2.5 mm, (c) 5 mm, (d) 10 mm, (e) 15 mm, and (f) 20 mm. The accelerating voltage has been taken equal to 300 kV, corresponding to a de Broglie wavelength of 1.968 pm.

The image wave function has been calculated by fast

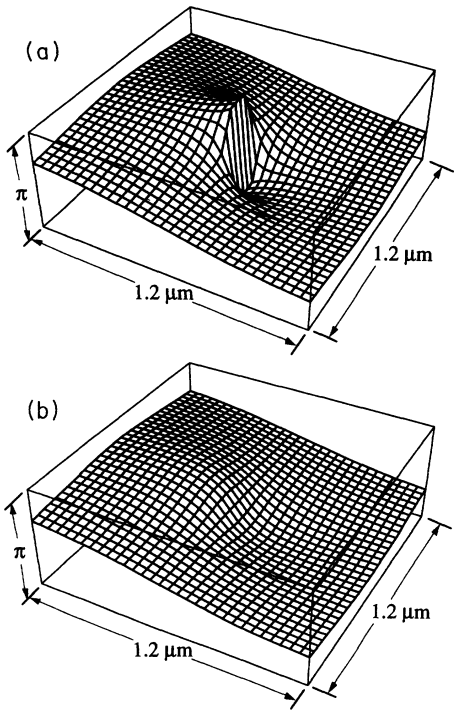

FIG. 4. Phase shift for 60-nm-thick specimens at 45° tilt. The flux tube model (a) shows the maximum phase difference of π, while for a London fluxon ($\lambda_L=30$ nm) the phase difference is smoothed and diminished (b).

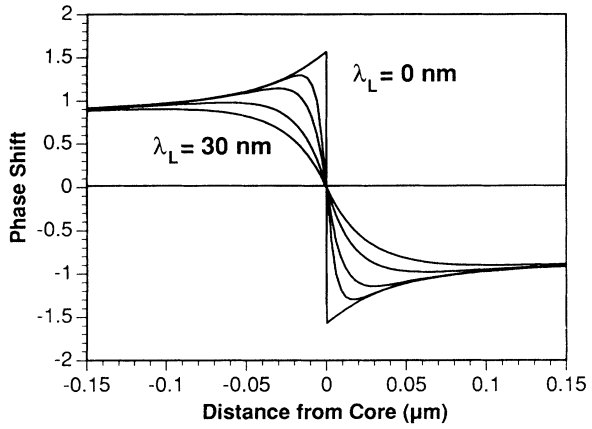

FIG. 5. Phase shift for different London lengths. The flux tube model and London fluxons (shown for $\lambda_L = 5$, 10, 20, and 30 nm) demonstrate that large λ_L values broaden the core.

Fourier transform (FFT) methods, on a square region centered at the fluxon having side 1.2 μm, i.e., $20\lambda_L$, with 256×256 sampling points. A linear phase term has been subtracted from the phase shift in order to avoid Fresnel diffraction effects from the edge parallel to the fluxon axis, where the phase has a $\pi/2$ jump owing to the truncation. Test calculations done by doubling both side and sampling points show no relevant differences.

A fluxon, being a perfect phase object, obviously shows no contrast in a zero-defocus image. Upon defocus, however, it can be ascertained from the calculated images that the fluxon has the appearance of a tiny globule, with two halves of bright and dark intensity aligned along the fluxon axis, as found experimentally (Fig. 2). Also low-contrast fringes surrounding the globules are present. Both the contrast and dimension of the globules increase with defocus distance: However, if the patterns are scaled proportionally to $(\lambda_L)^{1/2}$, it can be ascertained that, apart from the contrast, they look very similar.

In the geometric optical approximation, the dimensions of the image, being proportional to the Lorentz deflection at the specimen, should increase linearly with the defocus distance, implying that at the defocuses investigated the image contrast and appearance are mainly wave-optical effects due to Fresnel diffraction.

Figure 7 shows another focal series calculated for the case of a specimen having London length 30 nm, thickness 150 nm, i.e., $5\lambda_L$, at the same values of the defocus as before, i.e., (a) 1 mm, (b) 2.5 mm, (c) 5 mm, (d) 10 mm, (e) 15 mm, and (f) 20 mm.

The following features should be noted: At low defocus a lengthening of the image along the fluxon axis is visible, reflecting the fact that the fluxon projected length is $2.5\times$ longer than before. However, at the largest defocus, this lengthening is buried in the diffraction

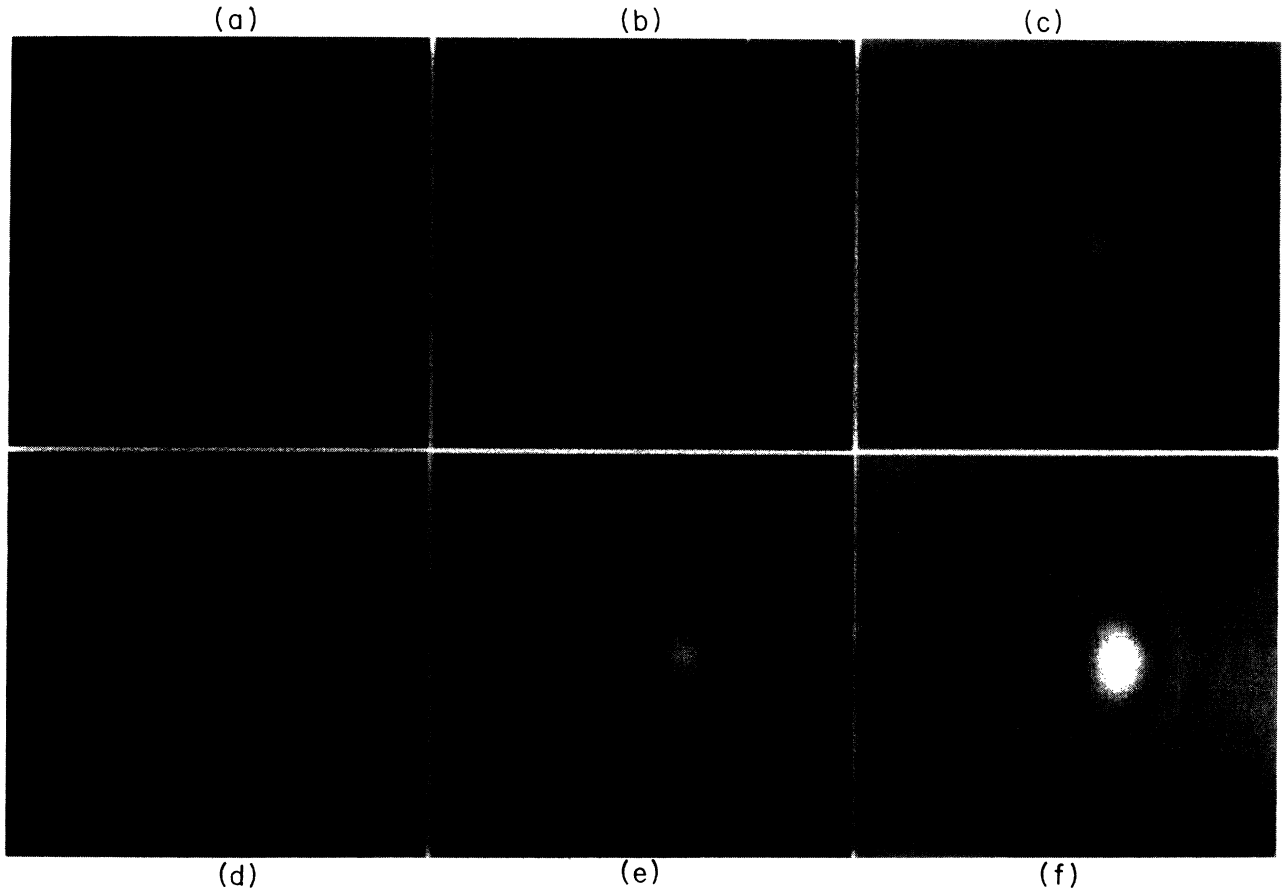

FIG. 6. Fluxon at different defocus distances. A specimen with $\lambda_L = 30$ nm, t of 60 nm at (a) 1 mm, (b) 2.5 mm, (c) 5 mm, (d) 10 mm, (e) 15 mm, and (f) 20 mm. The images measure 1.2 μm on each side.

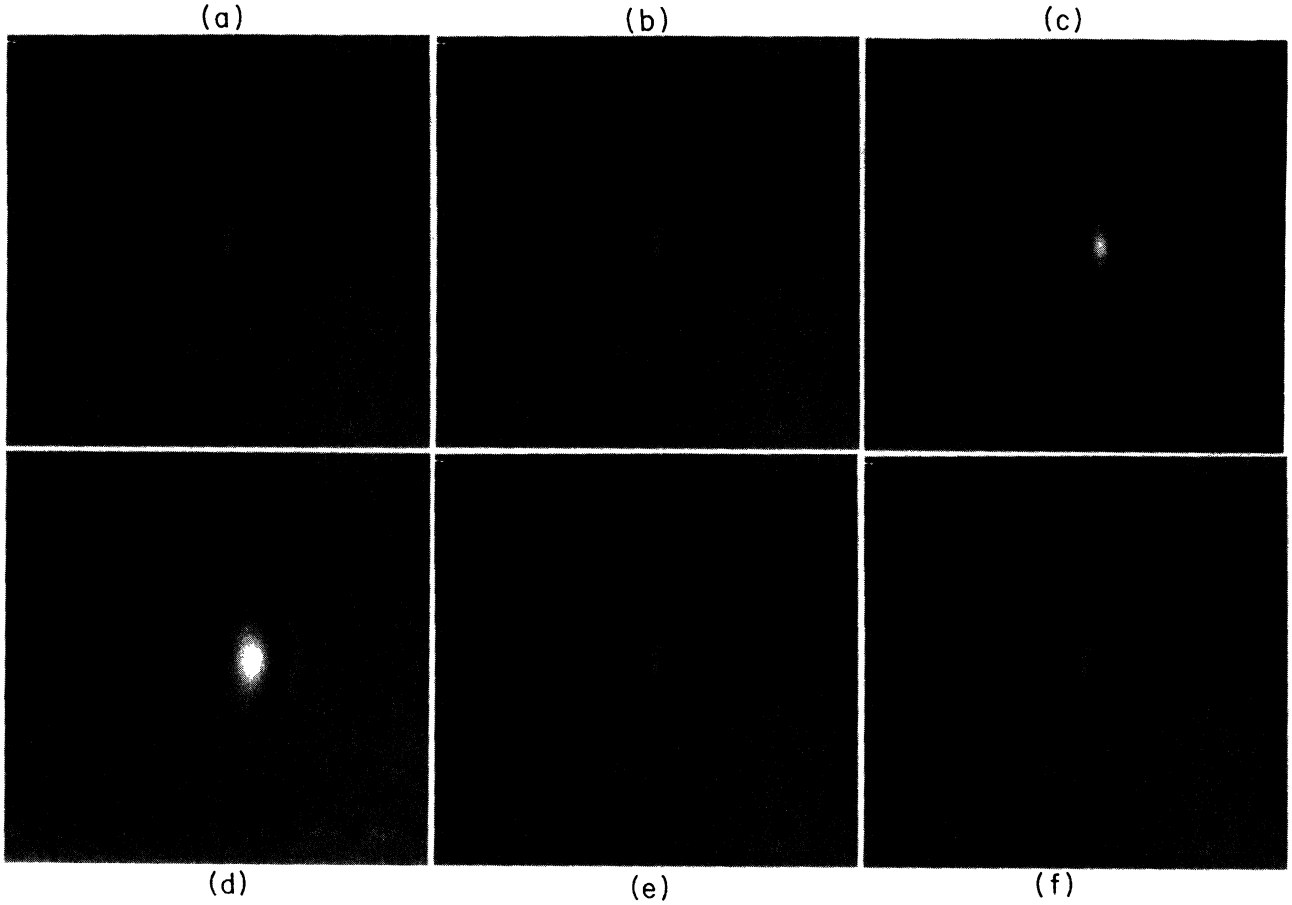

FIG. 7. Fluxon at different defocus distances. A specimen with $\lambda_L = 30$ nm, t of 150 nm at (a) 1 mm, (b) 2.5 mm, (c) 5 mm, (d) 10 mm, (e) 15 mm, and (f) 20 mm. Compare the vortex elongation in (a) and (b) with Fig. 2(a). The images measure 1.2 μm on each side.

broadening and can no longer be detected, so that the overall patterns are very similar to the previous one, apart from a variation of the intensity. This suggests that the lengthening observed in the experimental pattern at the lowest defocus [Fig. 2(a)] may be attributed to a specimen-dependent effect due to the thickness.

It should also be remarked that the 20-mm images in Figs. 6 and 7 begin to suffer from edge effects due to aliasing of the sampling array causing some faint subsidiary fringes at the edge of the images. These effects can be removed by increasing the side length (from 1.2 μm) in the calculations, however at the expense of computation time. Furthermore, as the images scale with $(\lambda_L)^{1/2}$, the general contrast features will remain unchanged.

Calculations have also been done for the cases of specimen thickness equal to λ_L and zero, i.e., negligible with respect to λ_L, and the general appearance of the patterns does not change significantly with respect to those reported in Fig. 6, apart from the contrast.

By defining the image contrast as

$$C = \frac{I_{\max} - I_{\min}}{I_{\max} + I_{\min}} , \tag{7}$$

we have plotted this quantity versus defocus for specimen thicknesses ranging stepwise from zero to $5\lambda_L$ and the results are summarized in Fig. 8. To make the data specimen independent, the defocus has been converted into the generalized defocus parameter, $p = \lambda Z_0 / \lambda_L^2$.

These curves show that the contrast increases from zero to a maximum with increasing defocus distance or the generalized defocus parameter and that this maximum depends on the specimen thickness. At the lower values of the abscissa, the trend of the curves is linear, as

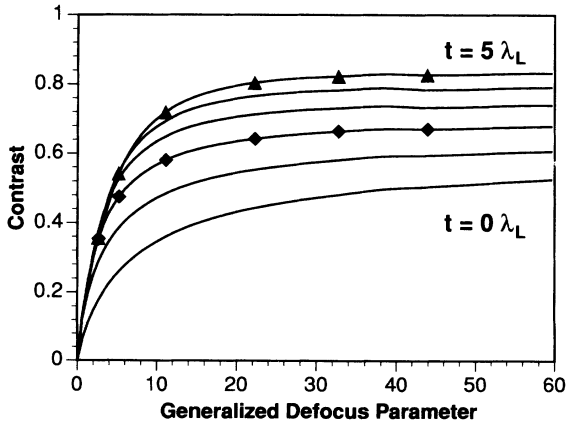

FIG. 8. Contrast variation of the fluxons with the generalized defocus parameter for different values of the thickness. Data points are shown for Fig. 6 (♦) and Fig. 7 (▲).

expected, because in this realm the geometric optical approximation becomes applicable.

The results summarized in Fig. 8 can be used to predict the out-of-focus contrast once the values of the various experimental parameters are known or guessed. For instance, if the London length is 10× larger, as with high-T_c superconductors, then for specimens transparent to 300-kV electrons the ratio t/λ_L is surely below 1 and the expected contrast should lie between the lowest two curves. However, in this case the generalized defocus parameter is 100×smaller than before, so that in order to have the same contrast, 100× larger defocus distances should be used. As practical defocus distances lie in the range 0–100 mm, this means that a much lower contrast should be expected than in the case of Nb as found experimentally.[2]

Further reduction of the contrast is expected from the fact that the present calculations do not take into account both the effects of elastic and inelastic scattering due to the specimen structure as well as the partial coherence of the illumination. For instance, these effects could be responsible for the fact that only the main globules are visible in the experimental images, whereas the low-contrast fringes surrounding them can be hardly detected in the original micrographs at the highest defocuses.

There is little doubt that inelastic scattering decreases the contrast in defocused images, but its magnitude is difficult to estimate because of the lack of experimental data. On the contrary, partial coherence effects can be accounted for by performing the convolution between the function describing the angular distribution of the electron source and the intensity in the image plane. However, with the high coherent field emission gun used in these experiments, this effect should not be very relevant so that inelastic scattering is mainly responsible for the loss of contrast.

This can be confirmed by analyzing the contrast of the diffraction fringes around the bend contours: In the thinner specimen regions and especially around the edge, a large number of diffraction fringes is visible, whereas in the thicker ones (such as that reported in Fig. 2) only one or two fringes are detectable.

V. CONCLUSIONS

Recently, we succeeded in observing the fluxon lattice in a thin specimen by means of transmission electron microscopy. Lorentz microscopy in particular has been employed to detect the fluxons and to study their dynamic behavior.[1,2]

In this technique, the phase shift produced by the fluxons in a tilted specimen is manifested in a defocused plane as spots of bright and dark contrast which have been interpreted in this work on the basis of a simple model taking into account the fluxon core structure. Also, novel contrast features have been predicted, such as faint fringes surrounding the globules and a lengthening of the images in thicker regions of the specimen, which seem to be confirmed by the experimental observations, although an unambiguous detection is masked by inelastic scattering and aberration effects. Moreover, as the core model employs a single parameter, it has been possible to draw general curves, which can be used to predict the contrast and to choose the best experimental conditions for a generic specimen.

Although a disadvantage of the Lorentz mode, as well as of the other standard phase contrast methods in electron microscopy,[20] is that it is very difficult to extract quantitative information from the experimental data, nonetheless the Lorentz micrographs indicate both the location and polarity of the fluxons and are of invaluable help for dynamic studies. We believe that classical Lorentz microscopy usefully supplements electron holography whenever quantitative data are not required.

ACKNOWLEDGMENTS

We would like to thank S. Kubota, S. Matsunami, and N. Moriya of Hitachi Ltd. for their technical assistance of the experiments. One of us (G.P.) would also like to express gratitude to colleagues at Lecce University, Italy for their discussions and support of the current work.

[1]K. Harada, T. Matsuda, J. Bonevich, M. Igarashi, S. Kondo, G. Pozzi, U. Kawabe, and A. Tonomura, Nature **360**, 51 (1992).

[2]K. Harada, T. Matsuda, H. Kasai, J. E. Bonevich, T. Yoshida, U. Kawabe, and A. Tonomura, Phys. Rev. Lett. **71**, 3371 (1993).

[3]J. E. Bonevich, K. Harada, T. Matsuda, H. Kasai, T. Yoshida, G. Pozzi, and A. Tonomura, Phys. Rev. Lett. **70**, 2952 (1993).

[4]C. Capiluppi, G. Pozzi, and U. Valdre, Philos. Mag. **26**, 865 (1972).

[5]V. Essman and H. Träuble, Phys. Lett. **24A**, 526 (1967).

[6]G. J. Dolan, F. Holtzberg, C. Field, and T. R. Dinger, Phys. Rev. Lett. **62**, 2184 (1989).

[7]H. F. Hess, R. B. Robinson, R. C. Dynes, J. M. Valles, and J. V. Waszczak, Phys. Rev. Lett. **62**, 214 (1989).

[8]J. Mannhart, J. Bosch, R. Gross, and R. P. Huebener, Phys. Rev. B **35**, 5267 (1987).

[9]A. Tonomura, Rev. Mod. Phys. **59**, 639 (1987).

[10]T. Matsuda, S. Hasegawa, M. Igarashi, T. Kobayashi, M. Naito, H. Kajiyama, J. Endo, N. Osakabe, A. Tonomura, and R. Aoki, Phys. Rev. Lett. **62**, 2519 (1989).

[11]T. Matsuda, A. Fukuhara, T. Yoshioka, S. Hasegawa, A. Tonomura, and Q. Ru, Phys. Rev. Lett. **66**, 457 (1991).

[12]T. Yoshida, T. Matsuda, and A. Tonomura, in *Proceedings of the 50th Annual Meeting of the Electr. Microsc. Society of America,* edited by G. W. Bailey (San Francisco Press, San Francisco, 1992), p. 68.

[13]C. A. Durán, P. L. Gammel, R. Wolfe, V. J. Fratello, D. J. Bishop, J. P. Rice, and D. M. Ginsberg, Nature **357**, 474 (1992).

[14]A. M. Chang, H. D. Hallen, L. Harriott, H. F. Hess, H. L. Kao, J. Kwo, R. E. Miller, R. Wolfe, and J. van der Ziel, Appl. Phys. Lett. **61**, 1974 (1992).
[15]A. Migliori and G. Pozzi, Ultramicroscopy **41**, 169 (1992).
[16]A. Migliori, G. Pozzi, and A. Tonomura, Ultramicroscopy **49**, 87 (1993).
[17]T. Kawasaki, T. Matsuda, J. Endo, and A. Tonomura, Jpn. J. Appl. Phys. **29**, L508 (1990).
[18]A. Fukuhara, K. Shingawa, A. Tonomura, and H. Fujiwara, Phys. Rev. B **27**, 1839 (1983).
[19]W. Glaser, Hand. Phys. **33**, 330 (1956).
[20]J. N. Chapman, J. Phys. D **17**, 623 (1984).

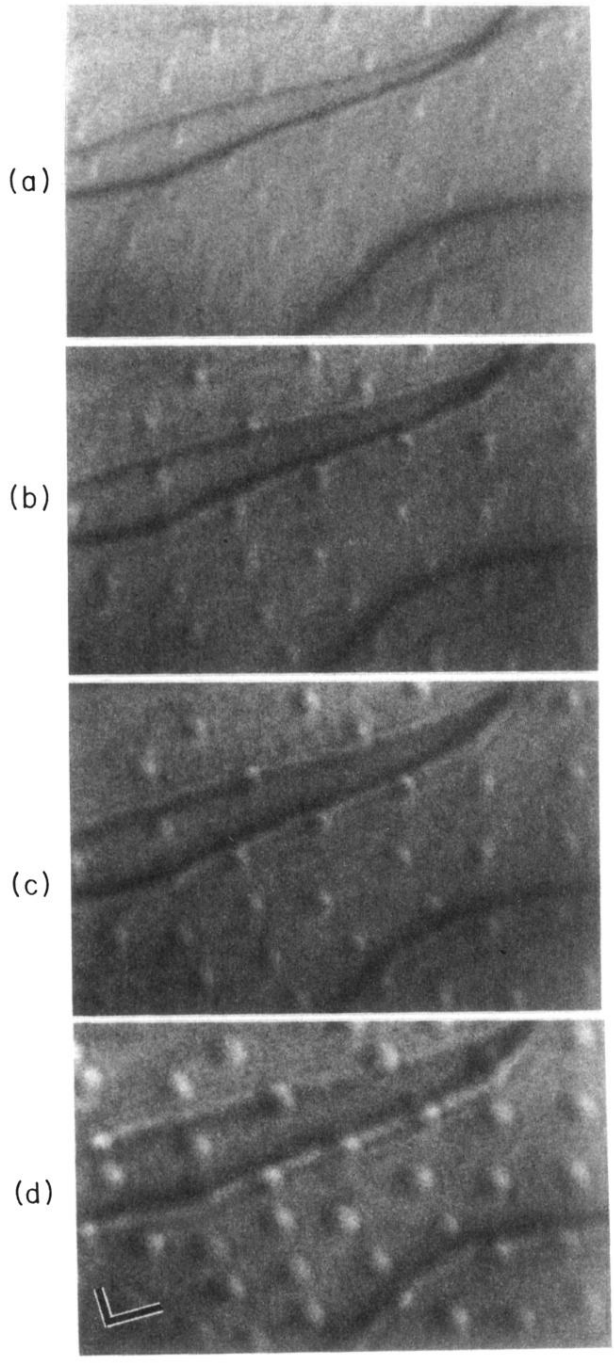

FIG. 2. Vortices in Nb at 4.5 K and 10 G. Through focus series (a)–(d) of 8, 15, 21, and 35 mm defocus. Individual vortices manifest themselves as globules of bright and dark contrast. Note that vortices in (a) appears slightly elongated as a result of the thickness of the specimen. Dark lines are bend contours in the thin foil. The scale bars indicate 0.5 μm.

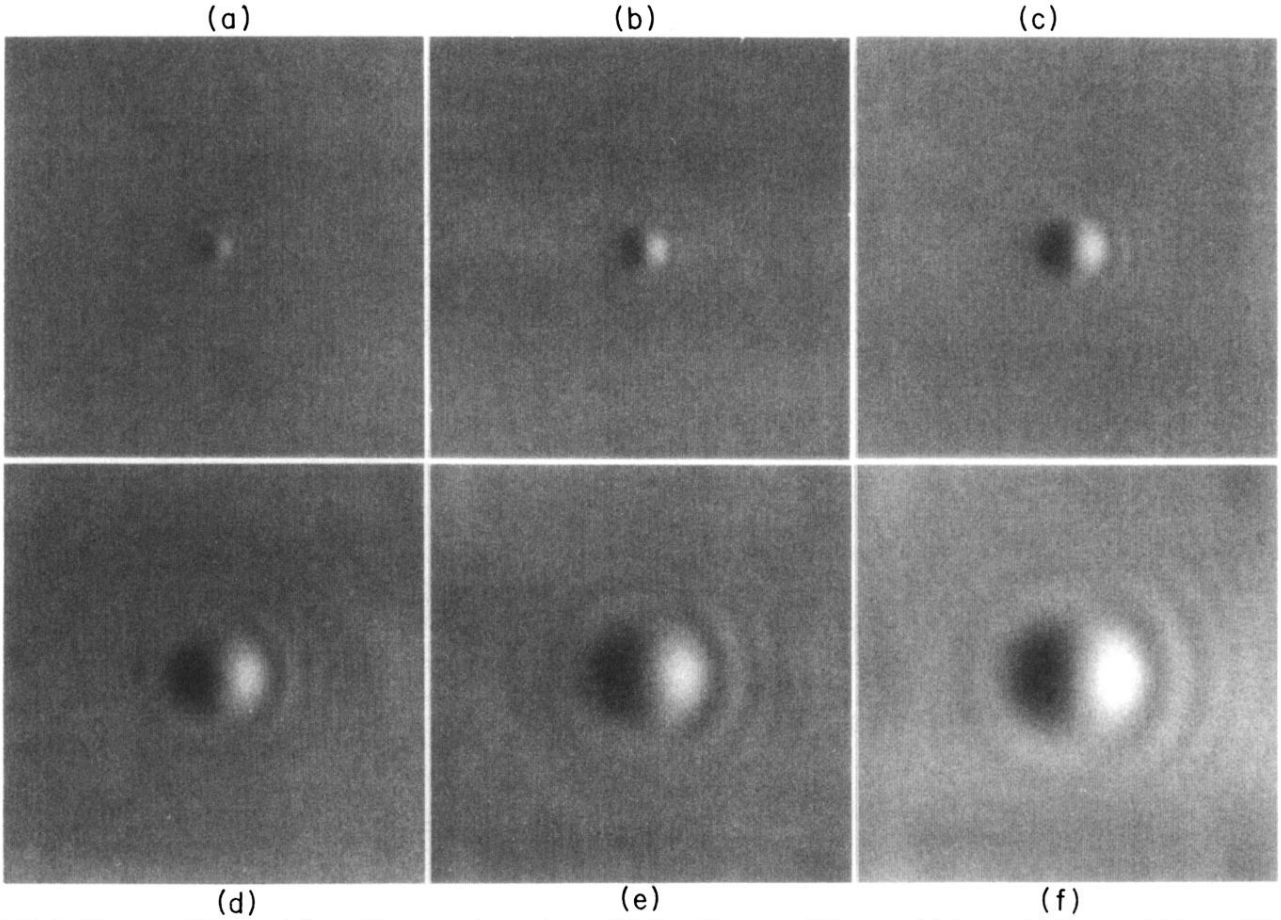

FIG. 6. Fluxon at different defocus distances. A specimen with $\lambda_L = 30$ nm, t of 60 nm at (a) 1 mm, (b) 2.5 mm, (c) 5 mm, (d) 10 mm, (e) 15 mm, and (f) 20 mm. The images measure 1.2 μm on each side.

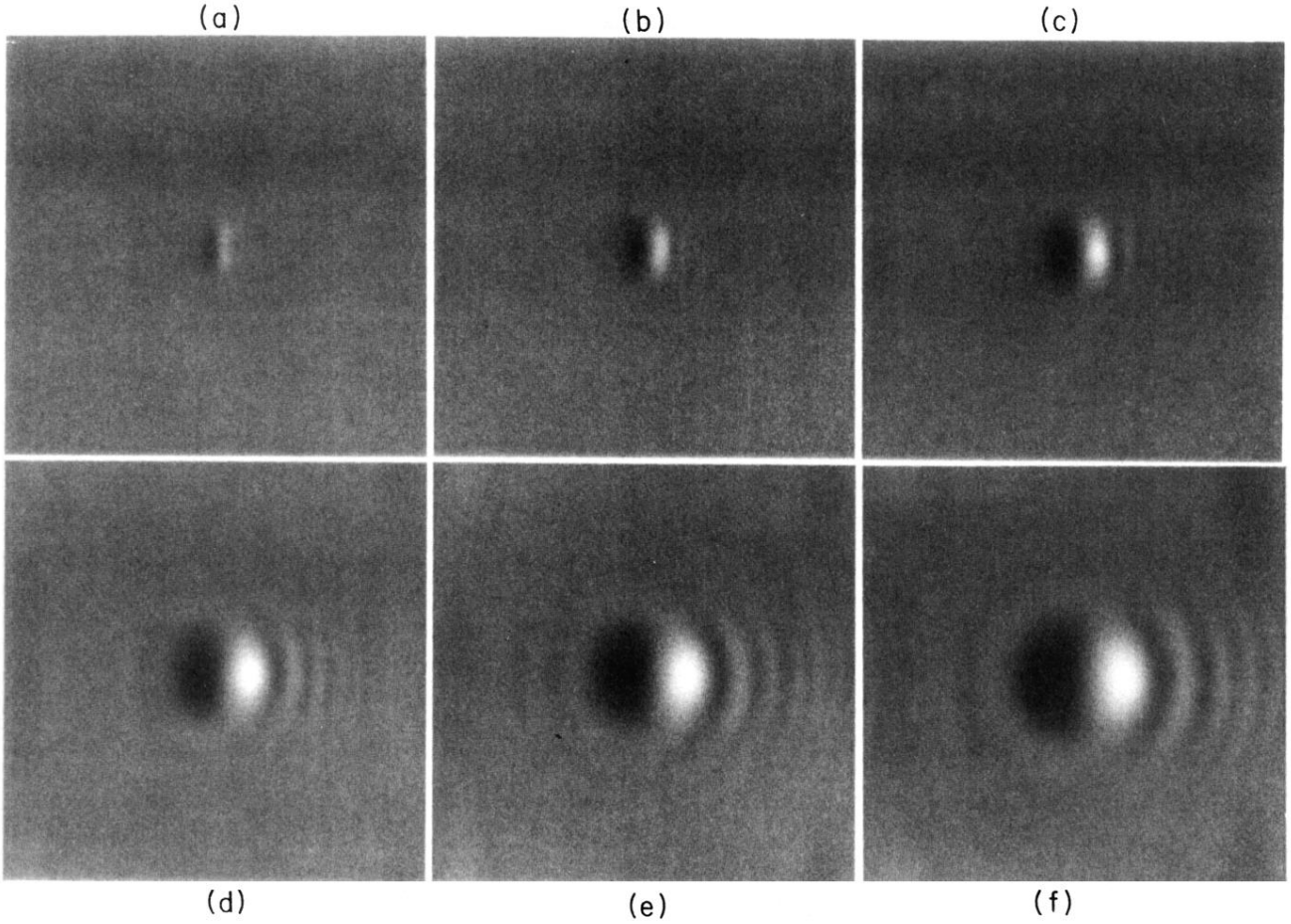

FIG. 7. Fluxon at different defocus distances. A specimen with $\lambda_L = 30$ nm, t of 150 nm at (a) 1 mm, (b) 2.5 mm, (c) 5 mm, (d) 10 mm, (e) 15 mm, and (f) 20 mm. Compare the vortex elongation in (a) and (b) with Fig. 2(a). The images measure 1.2 μm on each side.